Force Control of an Underactuated Tendon-Driven Manipulator

Nicolas J.S. Testard, Christine Chevallereau, Philippe Wenger

Force control of an underactuated tendon-driven manipulator

Nicolas J.S. Testard[1], Christine Chevallereau[2], and Philippe Wenger[2]

[1]LIRMM, University of Montpellier, CNRS, Montpellier, France, nicolas.testard@lirmm.fr
[2]Nantes Université, École Centrale Nantes, CNRS, LS2N, UMR 6004, F-44000 Nantes, France

***Abstract*—This paper investigates the application of force controls on a tendon-driven underactuated robotic arm. A direct use of classical hybrid force/motion control based on computed torque control can lead to instability for this type of system. Reformulating the hybrid force/motion control using the pseudo computed torque control (PCTC) framework leads to a stable control strategy. Finally, it is shown that applying admittance control in combination with PCTC also results in stable behavior when exerting a force against a wall or in a cobotics context. These results are then validated through experimentation.**

***Index Terms*—Underactuated robots, Tendon-driven, Force control, Stability study**

I. Introduction

NATURE often inspires new technologies. The works of [1] and [2] introduce robots inspired by the bird neck. Since birds lack arms, they use their neck and beak to grasp and manipulate objects. These robots consist of stacked anti-parallelogram joints (Fig. 1). These joints exhibit coupled translational and rotational motion corresponding to the rolling of one ellipse over another [3], mimicking the motion between bird neck vertebrae. Also called X-joints, they are actuated by cables pulling on both sides of the joint, reproducing the action of muscles and tendons. In antagonistic actuation, these cables are referred to as tendons.

The robot presented in [2] has three X-joints and four tendons, allowing independent joint control. In contrast, the robot studied here has more X-joints than tendons, so several joints share the same tendons, making the system underactuated (Fig. 2). As shown in [4], increasing the number joints without increasing the number of tendons increases the robot workspace. Underactuation also enables adaptation to environmental obstacles [5]. With many underactuated X-joints, these robots resemble tendon-driven continuum robots [6], [7], which use a deformable backbone actuated by tendons attached at its ends. However, due to underactuation, [8] shows that computed torque control (CTC) may become unstable. Depending on the controlled variables, the system exhibits non-minimum phase behavior [9]. Similar instabilities were reported for flexible robots [10] and underactuated cable-driven parallel robots [11]. To regulate the end-effector (EE) position, pseudo computed torque control (PCTC), inspired by CTC, was proposed and exhibits a large stability domain [5].

Robotic arms may also need to apply forces or interact with users, requiring force rather than position control. In cable-driven robots this is challenging because cable tensions must remain positive. [12] reviews several force control strategies, including impedance control, admittance control, and hybrid force/motion control (HFMC). Impedance and admittance control, introduced by Hogan [13], regulate the applied EE force from position errors to ensure compliant behavior. The main difference is that impedance control outputs motor torques, while admittance control generates reference positions.

Impedance control has been applied to tendon-driven hands with fully actuated [14] and underactuated fingers [15], where it is implemented at the joint level. It has also been applied to the EE of a tendon-driven continuum robot [16], where robot dynamics are treated as disturbances rather than inverted in the control. However, impedance control requires an accurate dynamic model [17], which is often unavailable for cable-driven robots. Admittance control does not have this limitation and has been implemented in fully actuated [18] and underactuated [19] cable-driven parallel robots, where a user guides the robot using a handle with a force sensor.

Unlike impedance or admittance control, HFMC separates force-controlled variables and position-controlled variables. It has been applied to continuum robots interacting with surfaces [20], [21]. In [20], the robot is tendon-driven but dynamics are not considered, whereas [21] inverts and linearizes the dynamics but uses secondary backbones instead of tendons.

Several controllers for constrained underactuated robots were proposed in [22], but their stability was not analyzed. Due to the robot underactuation, control stability must be carefully verified. Lyapunov analysis [23] is commonly used, although identifying a suitable Lyapunov function can be difficult. In some cases, the total system energy may serve as a Lyapunov candidate [24]. Another approach uses the Laplace domain [25]: for linear multiple-input multiple-output (MIMO) systems, stability can be studied through the poles of the transfer matrix. Nonlinear systems can be linearized around an equilibrium point, and if the linearized system is stable, the Lyapunov indirect method theorem ensures local asymptotic stability [26].

The tendon-driven underactuated structures studied here are promising for robots with modulable stiffness suitable for human–robot interaction, making force control essential. However, classical dynamic control is unstable for underactuated X-joint robots [5], [8]. Similarly, [27] showed that HFMC suffers from the same stability issues as CTC. While selecting appropriate outputs can mitigate instability in position control, this approach is ineffective for force control since the controlled directions are imposed by the environment. Therefore, classical force control strategies cannot be directly applied. The main contribution of this paper is the development of HFMC and admittance control strategies based on the PCTC

framework and applied at the EE. Their large stability domain is demonstrated by analyzing the transfer matrix of the linearized system. These results also highlight challenges likely to arise in tendon-actuated continuum robots.

The remainder of this paper is organized as follows. Section II presents the robot. Section III introduces the proposed HFMC based on PCTC and analyzes its stability. Section IV presents admittance control combined with PCTC for two scenarios: force application against a wall and cobotics. Experimental validation of both strategies is given in Section V. Section VI discusses the limitations of the presented control strategies, and Section VII concludes the paper.

II. Presentation of the Robot

A. General presentation and dynamic model

The studied planar robot consists of a stack of X-joints, illustrated in Fig. 1. The robot configuration is defined by the joint vector $\boldsymbol{\alpha}$ that contains the angles α_i between the upper and lower bars of each X-joint. Each joint is actuated by two antagonistic tendons of length l_j, which are pulled by motors. Figure 2 presents the robot under study. It consists of $N_j = 4$ joints and $N_c = 3$ tendons. The blue tendon pulls all the joints on one side, while the other two tendons each pull two successive joints on the opposite side. The green tendon passes through the first two joints in a direction nearly parallel to a diagonal bar, applying a negligible torque to the joint. This tendon routing was selected based on the findings of [4]. It can be observed that the robot is underactuated. Specifically, since two joints are actuated by the same tendons, they cannot be controlled independently. In general, with N_c tendons, only $N_c - 1$ degrees of freedom (DoFs) can be controlled [28], with the remaining DoF being used to maintain positive tension in the tendons. Thus, only 2 DoFs can be controlled on the robot shown in Fig. 2. Additionally, in this figure, it can be observed that springs are placed in parallel with the tendons to ensure a stable equilibrium configuration at rest, i.e., when no tension is applied to the tendons. An offset h_o is also considered at the EE.

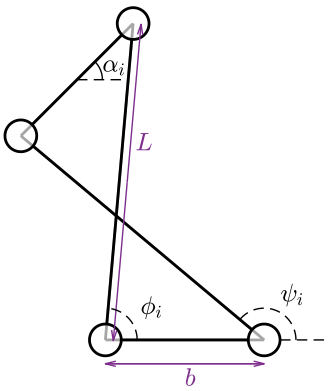

Fig. 1. X-joint kinematic representation. The joint has one degree of freedom defined as the angle α_i between the upper and lower bar.

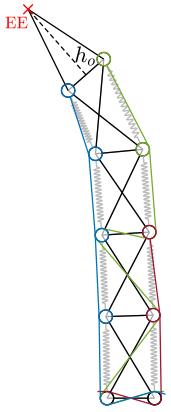

Fig. 2. Robot with 4 X-joints and 3 tendons with an offset. Springs in parallel of the tendons allow the robot to have a stable equilibrium configuration at rest.

We define $\boldsymbol{q}$ as the vector of controlled variables of the robot with dimension $N_c - 1$. In this paper, these controlled variables correspond to the EE position (x_{EE}, y_{EE}), and we will assume that the external forces applied to the robot act only at this point. The kinematic relationships between these controlled variables and the robot joint angles can be expressed as:

$$\boldsymbol{q} = \boldsymbol{g}_q(\boldsymbol{\alpha}) \tag{1}$$

$$\dot{\boldsymbol{q}} = \mathbf{J}(\boldsymbol{\alpha})\dot{\boldsymbol{\alpha}} \tag{2}$$

$$\ddot{\boldsymbol{q}} = \mathbf{J}(\boldsymbol{\alpha})\ddot{\boldsymbol{\alpha}} + \dot{\mathbf{J}}(\boldsymbol{\alpha}, \dot{\boldsymbol{\alpha}})\dot{\boldsymbol{\alpha}} \tag{3}$$

where $\mathbf{J}(\boldsymbol{\alpha}) = \frac{\partial \boldsymbol{g}_q}{\partial \boldsymbol{\alpha}}(\boldsymbol{\alpha})$ and $\boldsymbol{g}_q(\boldsymbol{\alpha})$ is defined for the EE position as [4]:

$$\begin{cases} x_{EE} = & -\sum_{i=1}^{n} \sin(\gamma_{i-1} + \frac{\alpha_i}{2}) \sqrt{L^2 - b^2 \cos^2(\frac{\alpha_i}{2})} - \sin(\gamma_n) h_o \\ y_{EE} = & \sum_{i=1}^{n} \cos(\gamma_{i-1} + \frac{\alpha_i}{2}) \sqrt{L^2 - b^2 \cos^2(\frac{\alpha_i}{2})} - \cos(\gamma_n) h_o \end{cases} \tag{4}$$

with $\gamma_0 = 0$ and $\gamma_n = \sum_{i=1}^{n} \alpha_i$.

The dynamic equation of the robot that links the joint acceleration $\ddot{\boldsymbol{\alpha}}$ to the tendon tensions $\boldsymbol{f}$ and the external forces $\boldsymbol{f}_q$ applied to the controlled variables can then be expressed as [1]:

$$\mathbf{M}(\boldsymbol{\alpha})\ddot{\boldsymbol{\alpha}} + \boldsymbol{d}(\boldsymbol{\alpha}, \dot{\boldsymbol{\alpha}}) = \mathbf{Z}(\boldsymbol{\alpha})\boldsymbol{f} + \mathbf{J}^{\top}(\boldsymbol{\alpha})\boldsymbol{f}_q \tag{5}$$

where:

- $\mathbf{M}(\boldsymbol{\alpha})$ is the robot inertia matrix,
- $\boldsymbol{d}(\boldsymbol{\alpha}, \dot{\boldsymbol{\alpha}})$ contains the gravitational effect, the springs effect, the centrifugal and coriolis effect and the friction. For this study, the friction model employed is viscous friction in the joint, defined as: $\boldsymbol{f}_r(\boldsymbol{\alpha}, \dot{\boldsymbol{\alpha}}) = -f_v \left(2 \left(\frac{\partial \boldsymbol{\phi}}{\partial \boldsymbol{\alpha}} \right)^2 + 2 \left(\frac{\partial \boldsymbol{\psi}}{\partial \boldsymbol{\alpha}} \right)^2 \right) \dot{\boldsymbol{\alpha}}$ where f_v is the friction constant and $\boldsymbol{\phi}$, resp $\boldsymbol{\psi}$, the vector of the angles between the left, resp. right, diagonal bar and the bottom bar. This corresponds to viscous friction at passive joints between the bars of the X-joints.
- $\mathbf{Z}(\boldsymbol{\alpha})$ is the matrix that relates tendon tensions to the torques they produce around the joint. Each term of this matrix is expressed by $\mathbf{Z}(\boldsymbol{\alpha})(i,j) = -\frac{\partial l_j(\alpha_i)}{\partial \alpha_i}$ where l_j is the length of the tendon j.

Coulomb friction on the wall is not considered here. Its impact will be discussed in Sect. VI.

III. Hybrid Force/Motion Control (HFMC)

The HFMC separates the controlled variables into position-controlled variables $\boldsymbol{q}_p$ and force-controlled variables $\boldsymbol{q}_f$: $\boldsymbol{q} = [\boldsymbol{q}_p^{\top}, \boldsymbol{q}_f^{\top}]^{\top}$.

The classical HFMC relies on the dynamic equation of the controlled variables, which relates the accelerations of the controlled variables $\ddot{\mathbf{q}}$ to the cable tensions $\mathbf{f}$ and the external forces $\mathbf{f}_q$ applied to the controlled variables. This equation is obtained by substituting Eq. (5) into Eq. (3):

$$\ddot{\boldsymbol{q}} = \mathbf{J}(\boldsymbol{\alpha})\mathbf{M}^{-1}(\boldsymbol{\alpha}) \left(\mathbf{Z}(\boldsymbol{\alpha})\boldsymbol{f} + \mathbf{J}^{\top}(\boldsymbol{\alpha})\boldsymbol{f}_q - \boldsymbol{d}(\boldsymbol{\alpha}, \dot{\boldsymbol{\alpha}}) \right) + \dot{\mathbf{J}}(\boldsymbol{\alpha}, \dot{\boldsymbol{\alpha}})\dot{\boldsymbol{\alpha}} \tag{6}$$

By applying position control on the acceleration of the position-controlled variables and force control on the force-controlled variables, it becomes possible to determine cable

tensions that allow tracking of both position and force references. However, we showed in [5] that inverting the dynamics for the control led to instabilities. We therefore propose to reformulate the HFMC by drawing inspiration from the PCTC approach, which we will name Pseudo Hybrid Force/Motion Control (PHFMC).

A. Implementation of the Pseudo Hybrid Force/Motion Control

Instead of directly inverting the dynamics, we invert the kinematics (Eq. (3)) and substitute it into Eq. (5):

$$\mathbf{M}\left(\mathbf{J}^{+}(\ddot{\boldsymbol{q}}-\dot{\mathbf{J}}\dot{\boldsymbol{\alpha}})+\mathbf{N}_{\mathbf{J}}\boldsymbol{\lambda}_{\alpha}\right)+\boldsymbol{d}=\mathbf{Z}\boldsymbol{f}+\mathbf{J}^{\top}\boldsymbol{f}_{q} \tag{7}$$

where $\mathbf{N_J}$ is the matrix whose columns form a basis of the null space of $\mathbf{J}$, and $\boldsymbol{\lambda}_\alpha$ is a vector of dimension $\dim(\boldsymbol{\alpha})-\dim(\boldsymbol{q})$. $\boldsymbol{\lambda}_\alpha = \mathbf{0}$ is chosen to ensure that $\ddot{\boldsymbol{\alpha}} = 0$ when $\ddot{\boldsymbol{q}}$ is desired to be zero in the control.

Equation (7) contains more equations than there are cables ($N_j > N_c$), and therefore cannot be solved directly to compute the cable tensions $\mathbf{f}$. To address this, the dynamic Eq. (7) can be left-multiplied by the matrix $\mathbf{P}$, which has dimensions $(N_c-1)\times N_j$ and whose rows are the N_c-1 dominant singular vectors of $\mathbf{Z}$. As shown in [29], the last singular value of the matrix $\mathbf{Z}$ is negligible compared to the others. This allows $\mathbf{PZ}$ to be a full rank $(N_c-1)\times N_c$ matrix. This leads to the following equation:

$$\mathbf{P}\left(\mathbf{M}\mathbf{J}^{+}(\ddot{\boldsymbol{q}}-\dot{\mathbf{J}}_{q}\dot{\boldsymbol{\alpha}})+\boldsymbol{d}\right)=\mathbf{P}\mathbf{Z}\boldsymbol{f}+\mathbf{P}\mathbf{J}^{\top}\boldsymbol{f}_{q} \tag{8}$$

A force sensor is mounted at the EE, allowing direct measurement of the force $\boldsymbol{f}_q$ applied to it. A corrected acceleration $\boldsymbol{w}_{q_p}$ is defined for the position-controlled variables, along with a corrected force $\boldsymbol{h}_{q_f}$ for the force-controlled variables :

$$\begin{cases} \boldsymbol{w}_{q_p} = & \ddot{\boldsymbol{q}}_p^d + K_p(\boldsymbol{q}_p^d - \boldsymbol{q}_p) + K_d(\dot{\boldsymbol{q}}_p^d - \dot{\boldsymbol{q}}_p) \\ & + K_i\int(\boldsymbol{q}_p^d - \boldsymbol{q}_p)dt \\ \boldsymbol{h}_{q_f} = & \boldsymbol{f}_{q_f}^d + K_{p2}(\boldsymbol{f}_{q_f}^d - \boldsymbol{f}_{q_f}) + K_{i2}\int(\boldsymbol{f}_{q_f}^d - \boldsymbol{f}_{q_f})dt \end{cases} \tag{9}$$

where K_p, K_d K_i, K_{p2} and K_{i2} are constant positive diagonal matrices and $\boldsymbol{f}_{q_f}$ is the force applied on the force-controlled variables.

We define the matrices $\mathbf{E}_p$ of dimension $\dim(\boldsymbol{q})\times\dim(\boldsymbol{q}_p)$ and $\mathbf{E}_f$ of dimension $\dim(\boldsymbol{q})\times\dim(\boldsymbol{q}_f)$. The entries of these matrices are 0 and 1 such that each row and each column contains exactly one 1 and $\mathbf{E}_p^\top\mathbf{E}_f = \mathbf{0}$, $\boldsymbol{q}_p = \mathbf{E}_p^\top\boldsymbol{q}$ and $\boldsymbol{q}_f = \mathbf{E}_f^\top\boldsymbol{q}$. It can also be written that $\boldsymbol{q} = \mathbf{E}_p\boldsymbol{q}_p + \mathbf{E}_f\boldsymbol{q}_f$.

We assume that the robot is in contact with a wall, with no desired motion of the EE perpendicular to the wall, and that friction $\boldsymbol{f}_{q_p}$ may act along the wall, affecting the position-controlled variables. By replacing $\ddot{\boldsymbol{q}}$ with $\mathbf{E}_p\boldsymbol{w}_{q_p}$, and $\boldsymbol{f}_q$ with $\mathbf{E}_f\boldsymbol{h}_{q_f} + \mathbf{E}_p\boldsymbol{f}_{q_p}$ in Eq. (8). The control equation is:

$$\mathbf{P}\left(\mathbf{M}\mathbf{J}^{+}(\mathbf{E}_p\boldsymbol{w}_{q_p}-\dot{\mathbf{J}}\dot{\boldsymbol{\alpha}})+\boldsymbol{d}\right)=\mathbf{P}\left(\mathbf{Z}\mathbf{f}+\mathbf{J}^{\top}\left(\mathbf{E}_f\boldsymbol{h}_{q_f}+\mathbf{E}_p\boldsymbol{f}_{q_p}\right)\right) \tag{10}$$

A Tension Distribution Algorithm (TDA) is applied:

$$\boldsymbol{f} = (\mathbf{P}\mathbf{Z})^{+}\boldsymbol{\Gamma} + \lambda_F\mathbf{n}_{\mathbf{PZ}} \tag{11}$$

where:

$$\boldsymbol{\Gamma} = \mathbf{P}\left(\mathbf{M}\mathbf{J}^{+}(\mathbf{E}_p\boldsymbol{w}_{q_p}-\dot{\mathbf{J}}\dot{\boldsymbol{\alpha}})+\boldsymbol{d}-\mathbf{J}^{\top}\left(\mathbf{E}_f\boldsymbol{h}_{q_f}+\mathbf{E}_p\boldsymbol{f}_{q_p}\right)\right) \tag{12}$$

λ_F is to ensure that all tendon tensions remain positive and $\mathbf{n_{PZ}}$ is the null space vector of $\mathbf{PZ}$. As observed in [5], the vector $\mathbf{n_{PZ}}$ contains strictly positive values for this type of robot. Therefore, it is possible to determine a value of λ_F such that all tensions are greater than a minimum threshold $f_{min} > 0$. In the control, at least one cable is maintained at this minimum tension.

The PHFMC scheme is illustrated in Fig. 3.

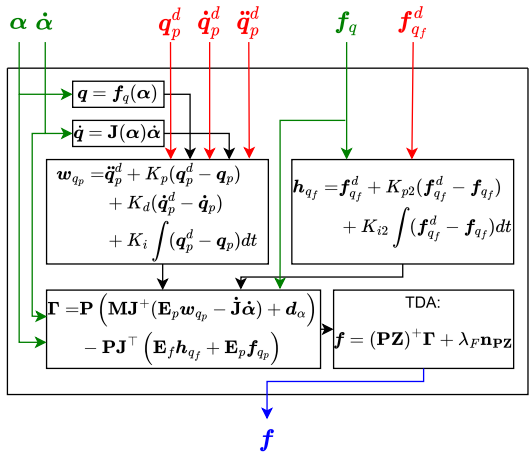

Fig. 3. Scheme of the PHFMC.

B. Stability equation of the PHFMC

1) Linearization of the dynamic model around an equilibrium configuration:

We consider a static equilibrium configuration with tendon tensions greater than or equal to a positive minimum tension f_{min}:

$$\boldsymbol{d}_\alpha(\boldsymbol{\alpha_0}, 0) = \mathbf{Z}(\boldsymbol{\alpha_0})\boldsymbol{f}_0 + \mathbf{J}^{\top}(\boldsymbol{\alpha}_0)\boldsymbol{f}_{q0} \tag{13}$$

To simplify the notations, we define: $\mathbf{Z} = \mathbf{Z}(\boldsymbol{\alpha_0})$, $\mathbf{J} = \mathbf{J}(\boldsymbol{\alpha}_0)$ et $\mathbf{M} = \mathbf{M}(\boldsymbol{\alpha}_0)$. The resulting linearized dynamic equation is:

$$\mathbf{M}\ddot{\boldsymbol{\alpha}}_* + \mathbf{D}\dot{\boldsymbol{\alpha}}_* + \mathbf{K}\boldsymbol{\alpha}_* = \mathbf{Z}\boldsymbol{f}_* + \mathbf{J}^{\top}\boldsymbol{f}_{q*} \tag{14}$$

where $\boldsymbol{\alpha}_* = \boldsymbol{\alpha} - \boldsymbol{\alpha}_0$, $\boldsymbol{f}_* = \boldsymbol{f} - \boldsymbol{f}_0$, $\boldsymbol{f}_{q*} = \boldsymbol{f}_q - \boldsymbol{f}_{q0}$, $\mathbf{K} = \frac{\partial\left(\boldsymbol{d}(\boldsymbol{\alpha},\dot{\boldsymbol{\alpha}}) - \mathbf{Z}(\boldsymbol{\alpha})\boldsymbol{f}_0 - \mathbf{J}^{\top}(\boldsymbol{\alpha})f_{q0}\right)}{\partial\boldsymbol{\alpha}}(\boldsymbol{\alpha}_0, \dot{\boldsymbol{\alpha}}_0)$ and $\mathbf{D} = \frac{\boldsymbol{d}(\boldsymbol{\alpha},\dot{\boldsymbol{\alpha}})}{\partial\dot{\boldsymbol{\alpha}}}(\boldsymbol{\alpha}_0, \dot{\boldsymbol{\alpha}}_0)$. Since we consider an initially static position, $\dot{\boldsymbol{\alpha}}_0 = 0$. The term $\mathbf{K}$ is influenced only by gravity, the springs, the tendon tensions, and the forces applied at the EE. The term $\mathbf{D}$ depends solely on viscous friction since Coulomb friction is undefined at $\dot{\boldsymbol{\alpha}}_0 = 0$ and cannot be linearized .

The TDA used in the control enforces a minimum tension f_{min} in one of the tendons, while allowing higher tensions in the remaining ones. We assume that the tension in this tendon locally remains at this minimum. This leads to the simplification $\mathbf{Z}\boldsymbol{f}_* = \mathbf{Z}_u\boldsymbol{u}$, where $\mathbf{Z}_u$ and the input control $\boldsymbol{u}$ represent $\mathbf{Z}$ and $\boldsymbol{f}_*$, respectively, without the column (resp. element) corresponding to the tendon that is at f_{min}.

$$\mathbf{M}\ddot{\boldsymbol{\alpha}}_* + \mathbf{D}\dot{\boldsymbol{\alpha}}_* + \mathbf{K}\boldsymbol{\alpha}_* = \mathbf{Z}_u\boldsymbol{u} + \mathbf{J}^\top \boldsymbol{f}_{q*} \tag{15}$$

Finally, by defining $\boldsymbol{q}_* = \boldsymbol{q} - \boldsymbol{q}_0$, the linearized kinematic equation is:

$$\boldsymbol{q}_* = \mathbf{J}\boldsymbol{\alpha}_* \tag{16}$$

2) Computation of the PHFMC transfer matrix:
Our goal is to express the transfer matrix between the input control $\boldsymbol{u}$ and the desired position and force ($\boldsymbol{q}_p^d$ and $\boldsymbol{f}_{q_f}^d$) and to analyze its poles to determine stability. To achieve this, we will first express the robot dynamics in the Laplace domain. Friction along the wall is not considered in the analysis ($\boldsymbol{f}_{q_p} = 0$ leading to $\mathbf{J}^\top \boldsymbol{f}_{q*} = \mathbf{J}^\top \mathbf{E}_f \boldsymbol{f}_{qf*}$).

Equation (15) in the Laplace domain becomes:

$$\mathbf{K}_D(s)\tilde{\boldsymbol{A}} = \mathbf{Z}_u\tilde{\boldsymbol{U}} + \left(\mathbf{E}_f^\top \mathbf{J}\right)^\top \tilde{\boldsymbol{F}}_{q_f} \tag{17}$$

where s is the Laplace variable, $\tilde{\boldsymbol{A}}$, $\tilde{\boldsymbol{U}}$, and $\tilde{\boldsymbol{F}}_{q_f}$ are $\boldsymbol{\alpha}_*$, $\boldsymbol{u}$, and $\boldsymbol{f}_{q_f*}$ in the Laplace domain, respectively, and $\mathbf{K}_D(s) = \mathbf{M}s^2 + \mathbf{D}s + \mathbf{K}$.

We suppose that the position of the force-controlled variables $\boldsymbol{q}_f$ of the robot do not change (e.g. in the case of a rigid wall). In other words, $\mathbf{E}_f^\top \mathbf{J}\tilde{\boldsymbol{A}} = 0$. Thus, from Eq. (17), we obtain:

$$\mathbf{E}_f^\top \mathbf{J}\left(\mathbf{K}_D(s)\right)^{-1}\left(\mathbf{Z}_u\tilde{\boldsymbol{U}} + \left(\mathbf{E}_f^\top \mathbf{J}\right)^\top \tilde{\boldsymbol{F}}_{q_f}\right) = 0 \tag{18}$$

and the relationship between $\tilde{\boldsymbol{U}}$ and $\tilde{\boldsymbol{F}}_{q_f}$ is:

$$\tilde{\boldsymbol{F}}_{q_f} = \mathbf{H}_{q_f}(s)\tilde{\boldsymbol{U}} \tag{19}$$

where:

$$\mathbf{H}_{q_f}(s) = -\left(\mathbf{E}_f^\top \mathbf{J}\left(\mathbf{K}_D(s)\right)^{-1}\left(\mathbf{E}_f^\top \mathbf{J}\right)^\top\right)^{-1} \mathbf{E}_f^\top \mathbf{J}\left(\mathbf{K}_D(s)\right)^{-1}\mathbf{Z}_u \tag{20}$$

Using Eq. (17), we also obtain the relationship between $\tilde{\boldsymbol{A}}$ and $\tilde{\boldsymbol{U}}$ and between $\tilde{\boldsymbol{Q}}_p$ (the Laplace transform of $\boldsymbol{q}_{p*}$) and $\tilde{\boldsymbol{U}}$:

$$\tilde{\boldsymbol{A}} = \mathbf{H}_\alpha(s)\tilde{\boldsymbol{U}}, \quad \tilde{\boldsymbol{Q}}_p = \mathbf{H}_{q_p}(s)\tilde{\boldsymbol{U}} \tag{21}$$

where

$$\begin{aligned}\mathbf{H}_\alpha(s) &= \left(\mathbf{K}_D(s)\right)^{-1}\left(\mathbf{Z}_u + \left(\mathbf{E}_f^\top \mathbf{J}\right)^\top \mathbf{H}_{q_f}(s)\right)\\ \mathbf{H}_{q_p}(s) &= \mathbf{E}_p^\top \mathbf{J}\mathbf{H}_\alpha(s)\end{aligned} \tag{22}$$

By defining $PID(s) = K_p + K_d s + K_i\frac{1}{s}$ and $PI(s) = K_{p2} + K_{i2}\frac{1}{s}$, the control Eq. (10) in the Laplace domain is (using Eq. (9)) :

$$\begin{aligned}&\mathbf{P}\left(\mathbf{D}s + \mathbf{K}\right)\tilde{\boldsymbol{A}} + \mathbf{P}\mathbf{M}\mathbf{J}^+\mathbf{E}_p\left(s^2\tilde{\boldsymbol{Q}}_p^d + PID(s)\left(\tilde{\boldsymbol{Q}}_p^d - \tilde{\boldsymbol{Q}}_p\right)\right)\\ &= \mathbf{P}\mathbf{Z}_u\tilde{\boldsymbol{U}} + \mathbf{P}\mathbf{J}^\top\mathbf{E}_f\left(\tilde{\boldsymbol{F}}_{q_f}^d + PI(s)\left(\tilde{\boldsymbol{F}}_{q_f}^d - \tilde{\boldsymbol{F}}_{q_f}\right)\right)\end{aligned} \tag{23}$$

Thus, by defining:

$$\mathbf{V}_{q_f 2}(s) = -\mathbf{P}\mathbf{J}^\top\mathbf{E}_f(\mathbf{I} + PI(s)) \tag{24}$$

$$\mathbf{V}_{q_p 2}(s) = \mathbf{P}\mathbf{M}\mathbf{J}^+\mathbf{E}_p(s^2\mathbf{I} + PID(s)) \tag{25}$$

$$\begin{aligned}\mathbf{V}_{u2}(s) =& \mathbf{P}\mathbf{M}\mathbf{J}^+\mathbf{E}_p PID(s)\mathbf{H}_{q_p}(s) + \mathbf{P}\mathbf{Z}_u\\ &- \mathbf{P}\mathbf{J}^\top\mathbf{E}_f PI(s)\mathbf{H}_{q_f}(s) - \mathbf{P}\left(\mathbf{D}s + \mathbf{K}\right)\mathbf{H}_\alpha\end{aligned} \tag{26}$$

the transfer matrix of the PHFMC is defined as:

$$\tilde{\boldsymbol{U}} = \mathbf{G}_1(s)\begin{bmatrix}\tilde{\boldsymbol{Q}}_p^d\\ \tilde{\boldsymbol{F}}_{q_f}^d\end{bmatrix} \tag{27}$$

where:

$$\mathbf{G}_1(s) = \mathbf{V}_{u2}^{-1}(s)\left[\mathbf{V}_{q_p 2}(s), \mathbf{V}_{q_f 2}(s)\right] \tag{28}$$

C. Stability results of the PHFMC

A vertical wall is assumed to be in contact with the EE, with $q_f = x_{EE}$, and the robot is expected to move along the wall, i.e., $q_p = y_{EE}$ ($\mathbf{E}_p = [1, 0]^\top$ and $\mathbf{E}_f = [0, 1]^\top$).

To study the stability of PHFMC as a function of the robot configuration, we can vary three interrelated parameters: the position of the wall, the force applied by the wall on the EE, and the position of the EE along the wall. We consider a wall placed at a distance -0.22 m from the robot base and a displacement of the EE along the wall within the range $y_{EE} \in [0.1,\ 0.35]$ m, as illustrated in Fig. 4. For a given force f_{q_f}, a minimum tension f_{min}, and a desired EE position $[x_{EE}^d, y_{EE}^d]$, the static equation (13) can be solved to determine the robot configuration in the following optimization scheme:

$$\begin{aligned}(\boldsymbol{\alpha}, \boldsymbol{f}) = &\min ||\boldsymbol{f}||\\ s.t. \quad &\begin{cases}\boldsymbol{d}(\boldsymbol{\alpha}) = \mathbf{Z}(\boldsymbol{\alpha})\boldsymbol{f} + \mathbf{E}_f^\top \mathbf{J}^\top(\boldsymbol{\alpha}) f_{q_f}\\ \boldsymbol{f}_q(\boldsymbol{\alpha}) = [x_{EE}^d, y_{EE}^d]^\top\\ \min(\boldsymbol{f}) \geq f_{min}\end{cases}\end{aligned} \tag{29}$$

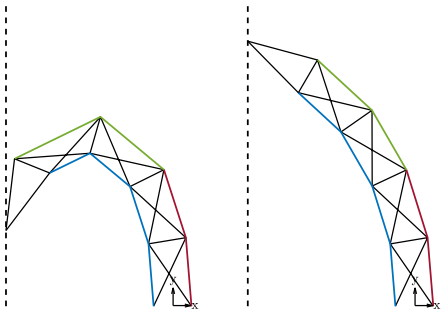

Fig. 4. Robot in contact with a wall at -0.22 m from the robot base with a vertical position of the EE of $y_{EE} = 0.1$ m (left) and $y_{EE} = 0.35$ m (right).

For the stability analysis, we use the design parameters of our prototype. The diagonal bar of the X-joint has a length of $L = 0.1$ m and a mass of 26 g, while the short bar has a length of $b = 0.05$ m and a mass of 162 g. The short bar is heavier because, in our prototypes, it consists of two parallel bars connected by two shafts that support the pulleys and an encoder used to determine the joint angle. The robot offset length is $h_o = 0.092$ m with a mass of 248 g, corresponding to the weight of a force sensor. The tendon routing is implemented using 7mm radius pulleys with bearings, which prevent friction between the tendon and the bars. The springs share the same free length $l_0 = 0.046$ m but have different stiffness values. From the first to the last joint, the stiffnesses are $k_r = [2000, 1750, 1250, 1000]$ N/m on the right and $k_l = [2000, 1750, 1250, 600]$ N/m on the left. The

asymmetry in stiffness between the right and left sides of the last joint is introduced to ensure that the robot does not rest in a straight configuration as represented in Fig. 2.

Figure 5 presents the stability results of the robot with a sampling of $y_{EE} \in [0.1,\ 0.35]$ m of 500 points for $f_{min} = 10$ N and $f_{q_p} = 5$ N. The considered friction constant is $f_v = 0.1$ N·m/(rad/s). The position-controlled variable gains are set to $K_p = 3\omega^2$, $K_d = 3\omega$, and $K_i = \omega^3$ with $\omega = 12$. This tuning is similar to that used in [5]. The gains for the force-controlled variables are chosen as $K_{p2} = 0.1$ and $K_{i2} = 10$. It is observed that the poles always have negative real parts, indicating that the control is stable along this trajectory. However, instabilities may appear if the gains of either the position-controlled or force-controlled variables controllers are greatly increased. Similar results are obtained for other robot design parameters, wall positions and force applied on it.

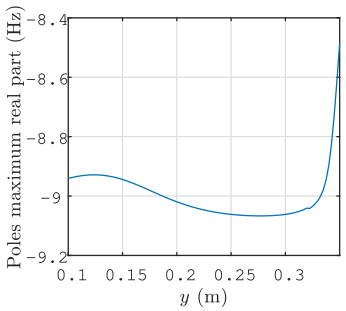

Fig. 5. Plot of the maximum real part of $\mathbf{G}_1(s)$ poles for $q_f = x_{EE}$ and $q_p = y_{EE}$ for a vertical wall at -0.22 m from the robot base with $f_{min} = 10$ N and $f_{q_p} = 5$ N. $K_{p2} = 0.1$, $K_{i2} = 10$, $K_p = 3\omega^2$, $K_d = 3\omega$ and $K_i = \omega^3$ with $\omega = 12$.

The relationship between $[\tilde{Q}_p, \tilde{F}_{q_f}]^\top$ and $[\tilde{Q}_p^d, \tilde{F}_{q_f}^d]^\top$ in the Laplace domain can also be expressed as:

$$\begin{bmatrix} \tilde{Q}_p \\ \tilde{F}_{q_f} \end{bmatrix} = \left[\mathbf{H}_{q_p}^\top(s), \mathbf{H}_{q_f}^\top(s)\right]^\top \mathbf{G}_1(s) \begin{bmatrix} \tilde{Q}_p^d \\ \tilde{F}_{q_f}^d \end{bmatrix} \tag{30}$$

It can be verified numerically that $\left[\mathbf{H}_{q_p}^\top(0), \mathbf{H}_{q_f}^\top(0)\right]^\top \mathbf{G}_1(0) = \mathbf{I}$, indicating that f_{q_f} and q_p correctly converge to their desired values under this control, as per the principle of the final value theorem [30].

Thus, the PHFMC introduced in this paper can be used to achieve stable force control of the EE for this type of underactuated robot.

IV. Admittance Control

A. Implementation of the admittance control with the PCTC

Admittance and impedance control do not separate position-controlled variables from force-controlled variables. These control strategies aim to impose a behavior of all controlled variables of the form:

$$\mathbf{M}_q^d(\ddot{\boldsymbol{q}} - \ddot{\boldsymbol{q}}^d) + \mathbf{D}_q^d(\dot{\boldsymbol{q}} - \dot{\boldsymbol{q}}^d) + \mathbf{K}_q^d(\boldsymbol{q} - \boldsymbol{q}^d) = \boldsymbol{f}_q \tag{31}$$

where $\mathbf{M}_q^d$, $\mathbf{D}_q^d$, and $\mathbf{K}_q^d$ represent the desired inertia, damping, and stiffness matrix, respectively. The control is asymptotically stable for continuous systems if these matrices are positive definite [31]. However, it is noted in [32] that, for discrete systems, in the scalar case, $\mathbf{M}_q^d$ cannot be smaller than half the robot mass for the control stability. In practice, these matrices are generally chosen to be diagonal in order to decouple the controlled variables.

Admittance control is used on robots controlled in position; in our case, the PCTC is employed. The inputs of the PCTC are reference positions $\boldsymbol{q}^r$. These reference positions are computed from the desired positions $\boldsymbol{q}^d$ and the forces measured by the sensor, in order to produce the desired error behavior:

$$\mathbf{M}_q^d(\ddot{\boldsymbol{q}}^r - \ddot{\boldsymbol{q}}^d) + \mathbf{D}_q^d(\dot{\boldsymbol{q}}^r - \dot{\boldsymbol{q}}^d) + \mathbf{K}_q^d(\boldsymbol{q}^r - \boldsymbol{q}^d) = \boldsymbol{f}_q \tag{32}$$

$\boldsymbol{q}^r$ is calculated at each time step by numerical integration as proposed by [18], noting i and $i-1$ the value at the current and previous step:

$$\begin{cases} \ddot{\boldsymbol{q}}_i^r = & \ddot{\boldsymbol{q}}_i^d + \left(\mathbf{M}_q^d\right)^{-1}\left(\boldsymbol{f}_{q,i} - \mathbf{D}_q^d(\dot{\boldsymbol{q}}_{i-1}^r - \dot{\boldsymbol{q}}_i^d) - \mathbf{K}_q^d(\boldsymbol{q}_{i-1}^r - \boldsymbol{q}_i^d)\right) \\ \dot{\boldsymbol{q}}_i^r = & \dot{\boldsymbol{q}}_{i-1}^r + \ddot{\boldsymbol{q}}_i^r dt \\ \boldsymbol{q}_i^r = & \boldsymbol{q}_{i-1}^r + \dot{\boldsymbol{q}}_i^r dt \end{cases} \tag{33}$$

where dt is the time step between two control updates. The PCTC is then used by taking into account the forces applied on the controlled variables:

$$\mathbf{P}\mathbf{Z}\boldsymbol{f} = \mathbf{P}\left(\mathbf{M}\mathbf{J}^+(\boldsymbol{w}_{q^r} - \dot{\mathbf{J}}\dot{\boldsymbol{\alpha}}) + \boldsymbol{d}(\boldsymbol{\alpha}, \dot{\boldsymbol{\alpha}}) - \mathbf{J}\boldsymbol{f}_q\right) \tag{34}$$

where $\boldsymbol{w}_{q^r} = \ddot{\boldsymbol{q}}^r + K_p(\boldsymbol{q}^r - \boldsymbol{q}) + K_d(\dot{\boldsymbol{q}}^r - \dot{\boldsymbol{q}}) + K_i \int (\boldsymbol{q}^r - \boldsymbol{q})dt$. The TDA is then applied:

$$\begin{aligned} \boldsymbol{f} = & (\mathbf{P}\mathbf{Z})^+ \mathbf{P}\left(\mathbf{M}\mathbf{J}^+(\boldsymbol{w}_{q^r} - \dot{\mathbf{J}}\dot{\boldsymbol{\alpha}}) + \boldsymbol{d}(\boldsymbol{\alpha}, \dot{\boldsymbol{\alpha}}) - \mathbf{J}\boldsymbol{f}_q\right) \\ & + \lambda_F \mathbf{n}_{\mathbf{PZ}} \end{aligned} \tag{35}$$

The scheme of the admittance control with the PCTC is described in Fig. 6.

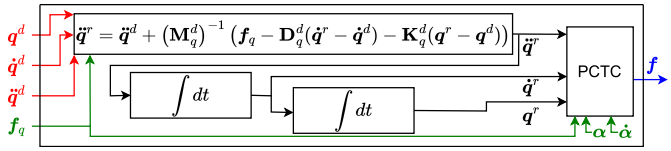

Fig. 6. Scheme of the admittance control with the PCTC.

This control strategy can be used to apply a desired force to a wall. In this context, we use the notation q_p for the variable controlled along the wall and q_f for the direction perpendicular to the wall. If the wall position is known, it is sufficient to set the desired position of the EE slightly beyond the wall by a distance δq_f perpendicular to the wall. A force will then be generated on the wall by the controller, with an amplitude of $K_{q_f}^d \delta q_f$ with $K_{q_f}^d$ the stiffness associated to q_f in the admittance control. By selecting appropriate values for $K_{q_f}^d$ and δq_f, the applied force on the wall can be precisely controlled.

Another possible application of this control method is in cobotics. By setting $\mathbf{K}_q^d = \mathbf{0}$ and specifying no desired trajectory, the robot can follow a path imposed by a user applying forces on the controlled variables. This type of control is particularly useful when aiming to move heavy loads with the assistance of the robot.

B. Stability of the admittance control with PCTC

Equation (32) becomes, in the Laplace domain:

$$\tilde{\boldsymbol{Q}}^r = \tilde{\boldsymbol{Q}}^d + (\mathbf{M}_q^d s^2 + \mathbf{D}_q^d s + \mathbf{K}_q^d)^{-1} \tilde{\boldsymbol{F}}_q \tag{36}$$

It can be observed that, when no force is applied to the EE, $\tilde{\boldsymbol{Q}}^r = \tilde{\boldsymbol{Q}}^d$, and thus the control transfer matrix corresponds to that of the PCTC, which was shown to have a large stability domain in [5].

1) Stability against a wall:

In this section, we consider that the robot applies a force against a vertical wall, as described in Section III-C. The PCTC Eq. (34) in the Laplace domain is:

$$\begin{aligned} \mathbf{PMJ}^+ \left(s^2 \tilde{\boldsymbol{Q}}^r + PID(s) \left(\tilde{\boldsymbol{Q}}^r - \tilde{\boldsymbol{Q}} \right) \right) = \\ \mathbf{PZ}_u \tilde{\boldsymbol{U}} + \mathbf{PJ}^\top \mathbf{E}_f \tilde{F}_{q_f} - \mathbf{P} \left(\mathbf{D}s + \mathbf{K} \right) \tilde{\boldsymbol{A}} \end{aligned} \tag{37}$$

We can therefore express the transfer matrix between the reference controlled variables $\tilde{\boldsymbol{Q}}^r$ and $\tilde{\boldsymbol{U}}$:

$$\tilde{\boldsymbol{U}} = \mathbf{G}_2(s) \tilde{\boldsymbol{Q}}^r \tag{38}$$

as :

$$\begin{aligned} \mathbf{G}_2(s) = \Big[\mathbf{PZ}_u + \mathbf{PJ}^\top \mathbf{E}_f \mathbf{H}_{q_f}(s) - \mathbf{P} \left(\mathbf{D}s + \mathbf{K} \right) \mathbf{H}_\alpha(s) \\ + \mathbf{PMJ}^+ PID(s) \mathbf{E}_p \mathbf{H}_{q_p}(s) \Big]^{-1} \left(\mathbf{PMJ}^+ (s^2 \mathbf{I} + PID(s)) \right) \end{aligned} \tag{39}$$

Equations (36) and (39) then allow us to express the relationship between $\tilde{\boldsymbol{Q}}^d$ and $\tilde{\boldsymbol{U}}$ as:

$$\tilde{\boldsymbol{U}} = \mathbf{G}_3(s) \tilde{\boldsymbol{Q}}^d \tag{40}$$

where

$$\mathbf{G}_3(s) = \left(\mathbf{I} - \mathbf{G}_2(s) (\mathbf{M}_q^d s^2 + \mathbf{D}_q^d s + \mathbf{K}_q^d)^{-1} \mathbf{E}_f \mathbf{H}_{q_f}(s) \right)^{-1} \mathbf{G}_2(s) \tag{41}$$

As in Section III-C, the wall is at -0.22 m from the base, $f_{min} = 10$ N and a force of 5 N is applied on the robot EE by the wall. Figure 7 presents the stability results of the admittance control for $\mathbf{K}_q^d = 100\mathbf{I}$, $\mathbf{D}_q^d = 20\mathbf{I}$, and $\mathbf{M}_q^d = 0.1\mathbf{I}$, $\mathbf{M}_q^d = 1\mathbf{I}$, or $\mathbf{M}_q^d = 10\mathbf{I}$. It can be observed that instabilities may arise when $\mathbf{M}_q^d$ is either too small (Fig. 7a) or too large (Fig. 7c). However, for certain values of $\mathbf{M}_q^d$, in this case, on the same order of magnitude as the weight of the robot, the control remains stable (Fig. 7b). The values of $\mathbf{D}_q^d$ and $\mathbf{K}_q^d$ do not appear to significantly affect stability, as long as they remain positive. Similar results are observed for other wall positions and other forces applied to the wall.

We can also express the relationship between $[\tilde{F}_{q_f}, \tilde{Q}_p]$ and $\tilde{\mathbf{q}}^d$ as:

$$\begin{bmatrix} \tilde{Q}_p \\ \tilde{F}_{q_f} \end{bmatrix} = \left[\mathbf{H}_{q_p}^\top(s), \mathbf{H}_{q_f}^\top(s) \right]^\top \mathbf{G}_3(s) \tilde{\mathbf{Q}}^d \tag{42}$$

We note $K_{q_f}^d$ the diagonal element of $\mathbf{K}_q^d$ associated with q_f. We obtain:

$$\left[\mathbf{H}_{q_p}^\top(0), \mathbf{H}_{q_f}^\top(0) \right]^\top \mathbf{G}_3(0) = \begin{bmatrix} 1 & 0 \\ 0 & -K_{q_f}^d \end{bmatrix} \tag{43}$$

This indicates that q_p converges to its desired position, and that applying a variation δq_f^d results in a change in the force applied on the robot EE of $-K_{q_f}^d \delta q_f^d$ (thus, the force exerted by the robot on the wall varies by $K_{q_f}^d \delta q_f^d$). Admittance control combined with PCTC can therefore be used to apply a force against a wall.

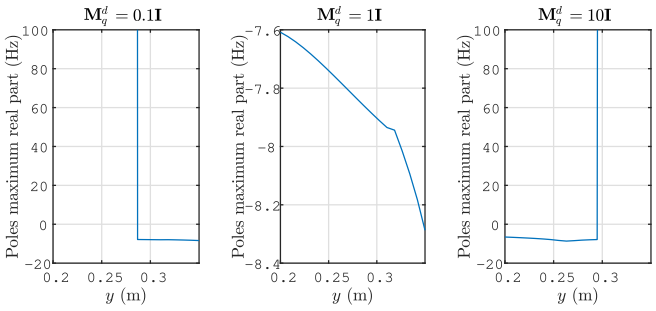

Fig. 7. Plots of the maximum real part of $\mathbf{G}_3(s)$ for a wall at $x_{EE} = -0.22$ m. $\mathbf{K}_q^d = 100\mathbf{I}$, $\mathbf{D}_q^d = 20\mathbf{I}$, and (a) $\mathbf{M}_q^d = 0.1\mathbf{I}$, (b) $\mathbf{M}_q^d = 1\mathbf{I}$, (c) $\mathbf{M}_q^d = 10\mathbf{I}$. $K_p = 3\omega^2$, $K_d = 3\omega$ and $K_i = \omega^3$ with $\omega = 12$.

2) Stability for cobotic application:

We now consider a cobotic application where $\mathbf{K}_q^d = \mathbf{0}$ and no desired control variables $\boldsymbol{q}^d$ are imposed. The admittance control in the Laplace domain then becomes:

$$\tilde{\boldsymbol{Q}}^r = \boldsymbol{H}_{q^r f_q}(s) \tilde{\boldsymbol{F}}_q \tag{44}$$

where

$$\boldsymbol{H}_{q^r f_q}(s) = (\mathbf{M}_q^d s^2 + \mathbf{D}_q^d s)^{-1} \tag{45}$$

The position of the EE evolves based on the amount of force applied to it, so the control input becomes: $\boldsymbol{i}_q = \int \boldsymbol{f}_q dt$. The goal is therefore to determine the transfer matrix between $\boldsymbol{u}$ and $\boldsymbol{i}_q$. By noting $\tilde{\boldsymbol{I}}_q$ the Laplace transform of $\boldsymbol{i}_q$, we have the relationship:

$$\tilde{\boldsymbol{F}}_q = s \tilde{\boldsymbol{I}}_q \tag{46}$$

The dynamic equations of the robot in this scenario are written as:

$$\begin{aligned} \tilde{\boldsymbol{A}} &= \mathbf{H}_{\alpha u}(s) \tilde{\boldsymbol{U}} + \mathbf{H}_{\alpha f_q}(s) \tilde{\boldsymbol{F}}_q \\ \tilde{\boldsymbol{Q}} &= \mathbf{H}_{qu}(s) \tilde{\boldsymbol{U}} + \mathbf{H}_{q f_q}(s) \tilde{\boldsymbol{F}}_q \end{aligned} \tag{47}$$

where

$$\begin{aligned} \mathbf{H}_{\alpha u}(s) = \boldsymbol{K}_D^{-1}(s) \mathbf{Z}_u, \quad \mathbf{H}_{\alpha f_q}(s) = \boldsymbol{K}_D^{-1}(s) \mathbf{J}^\top \\ \mathbf{H}_{qu}(s) = \mathbf{J} \mathbf{H}_{\alpha u}(s), \quad \mathbf{H}_{q f_q}(s) = \mathbf{J} \mathbf{H}_{\alpha f_q}(s) \end{aligned} \tag{48}$$

The PCTC equation in the Laplace domain yields:

$$\begin{aligned} \mathbf{PMJ}^+ \left(s^2 \tilde{\boldsymbol{Q}}^r + PID(s) \left(\tilde{\boldsymbol{Q}}^r - \tilde{\boldsymbol{Q}} \right) \right) = \\ \mathbf{PZ}_u \tilde{\boldsymbol{U}} + \mathbf{PJ}^\top \tilde{\boldsymbol{F}}_q - \mathbf{P} \left(\mathbf{D}s + \mathbf{K} \right) \tilde{\boldsymbol{A}} \end{aligned} \tag{49}$$

We can therefore express the relationship between $\tilde{\boldsymbol{U}}$ and $\tilde{\boldsymbol{I}}_q$ as:

$$\tilde{\boldsymbol{U}} = \mathbf{G}_4(s) \tilde{\boldsymbol{I}}_q \tag{50}$$

where:

$$\begin{aligned} \mathbf{G}_4(s) = \\ \left(\mathbf{PZ}_u - \mathbf{P} \left(\mathbf{D}s + \mathbf{K} \right) \mathbf{H}_{\alpha u}(s) + \mathbf{PMJ}^+ PID(s) \mathbf{H}_{qu}(s) \right)^{-1} \\ \left[-\mathbf{PJ}^\top + \mathbf{P} \left(\mathbf{D}s + \mathbf{K} \right) \mathbf{H}_{\alpha f_q}(s) + \right. \\ \left. \mathbf{PMJ}^+ \left((s^2 \mathbf{I} + PID(s)) \boldsymbol{H}_{q^r f_q}(s) - PID(s) \mathbf{H}_{q f_q}(s) \right) \right] s \end{aligned} \tag{51}$$

We study the stability of the control over a set of robot configurations. These configurations are defined by $\alpha_1 \in [-90°, 90°]$ and $\alpha_3 \in [-90°, 90°]$, each sampled over 100 points. We define $f_{min} = 10$ N and assume that no external force is initially applied to the EE ($\boldsymbol{f}_q = \mathbf{0}$). The values of α_2, α_4, and $\boldsymbol{f}$ are then computed for each configuration through the following optimization:

$$(\alpha_2, \alpha_4, \boldsymbol{f}) = \min ||\boldsymbol{f}|| \quad s.t. \quad \begin{cases} \boldsymbol{d}(\alpha_2, \alpha_4) = \mathbf{Z}(\alpha_2, \alpha_4)\boldsymbol{f} \\ \min(\boldsymbol{f}) \geq f_{min} \end{cases} \tag{52}$$

The results of the pole analysis of $\mathbf{G}_4(s)$ for each of these configurations are presented in Fig. 8. It can be observed that there are a few configurations where the maximum real part of the transfer matrix is positive (indicating instability) but for the majority of configurations, it is negative (indicating stability). The instability points of the control are located around kinematic singularities of the controlled variables. In this cobotic context, $\boldsymbol{M}_q$ and $\boldsymbol{D}_q$ have no influence on stability as long as they remain positive definite.

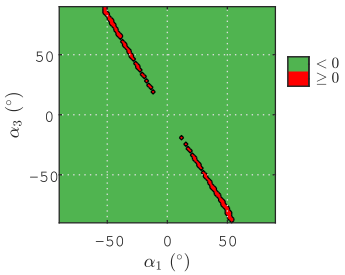

Fig. 8. Plot of maximum real part sign of $\mathbf{G}_4(s)$ poles for $M_q = 2\mathbf{I}$ and $M_q = 40\mathbf{I}$. $K_p = 3\omega^2$, $K_d = 3\omega$ and $K_i = \omega^3$ with $\omega = 12$.

Using Eq. (47), the transfer matrix between $\boldsymbol{q}$ and $\boldsymbol{i}_q$ can then be expressed as:

$$\tilde{\boldsymbol{Q}} = \left(\mathbf{H}_{\alpha u}(s)\mathbf{G}_4(s) + s\mathbf{H}_{\alpha f_q}(s)\right)\tilde{\boldsymbol{I}}_q \tag{53}$$

$s\boldsymbol{H}_{\alpha f_q}(s)$ is equal to the zero matrix when $s = 0$, and $\boldsymbol{H}_{\alpha u}(0)\mathbf{G}_4(0) = \boldsymbol{D}_q^{-1}$. It can be noted that this relationship between $\boldsymbol{q}$ and $\boldsymbol{i}_q$ is the same as that between $\dot{\boldsymbol{q}}$ and $\boldsymbol{f}_q$:

$$s\tilde{\boldsymbol{Q}} = \left(\mathbf{H}_{\alpha u}(s)\mathbf{G}_4(s) + s\mathbf{H}_{\alpha f_q}(s)\right)\tilde{\boldsymbol{F}}_q \tag{54}$$

Thus, applying a constant force on the EE results in a constant velocity $\boldsymbol{D}_q^{-1}\boldsymbol{f}_q$ of the EE, which is the expected behavior under admittance control. Therefore, the use of admittance control with PCTC in a cobotic context also leads to a stable control strategy.

V. Experiments

Simulations presented in [33] showed that these control laws remain stable during contact with a wall. This section presents the experiments validating these theoretical results on control stability in the different contexts previously described, for the robot with 4 X-joints and 3 tendons shown in Fig. 2.

A. Presentation of the prototype

It can be observed that, in Fig. 1, the diagonal bars intersect. In practice, the three-dimensional assembly allows us to place the diagonal bars on different planes, as shown in Fig. 9. Similarly, the tendons and springs are also positioned on different planes.

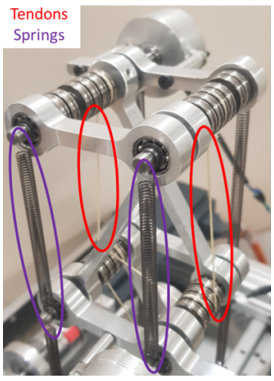

Fig. 9. X-joint assembly.

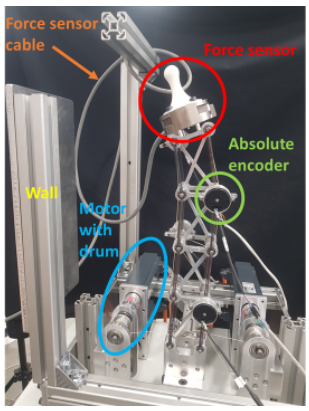

Fig. 10. Prototype.

The prototype setup is shown in Fig. 10. The tendons are driven by gearless Beckhoff motors (with an inertia of 52×10^{-6} kg·m^2) through a drum with a radius of 13 mm. These motors can generate tensions up to 92.3 N, and a minimum tendon tension of $f_{min} = 10$ N is chosen.

Absolute Heidenhain ECI 1119 encoders are mounted on each X-joint to measure the angle ϕ_i or ψ_i between a diagonal bar and the top bar. These measurements are used to compute the joint angle α_i. To ensure better mass distribution, the encoders are alternately placed in front on the right side or behind on the left side of each X-joint. Each joint velocity $\dot{\alpha}_i$ is then obtained by numerical differentiation and filtered using a third-order Butterworth infinite impulse response (IIR) filter with a cutoff frequency of 30 Hz. The position and velocity of the end effector are then computed using Eqs. (1) and (2).

A 6-axis Omega160 IP60 force sensor with a rounded tip is mounted at the robot EE to interact with the wall or the user. This sensor is connected to the computer via a relatively heavy and stiff cable, which may affect the robot performance. To minimize these disturbances, the cable is suspended over the robot. The forces measured with the sensor are also filtered using the same filter as for the joint velocities.

Finally, a removable wall is placed to the left of the robot at a distance of -0.22 m from the robot base.

B. Experiments with the PHFMC

The PHFMC is used here with $q_p = y_{EE}$ and $q_f = x_{EE}$, so as to apply a force on the wall while moving along it. We set $K_p = 3\omega^2\mathbf{I}$, $K_d = 3\omega\mathbf{I}$, and $K_i = \omega^3\mathbf{I}$ with $\omega = 12$, $K_{p2} = 0.1$ and $K_{i2} = 10$. The control update frequency is 1000 Hz. The robot is not in contact with the wall at the beginning of the experiment and is brought into contact using a PCTC. Once the sensor is in contact with the wall, the PHFMC is used to apply a force of 3 N against the wall and to impose a downward motion, followed by an upward motion. At the end

of the motion, a PCTC is used to break contact with the wall. Under the PHFMC, x^d_{EE} is not used for the tendon tension computation. However, it is still defined throughout the motion to trigger the switch back to the PCTC when $x^d_{EE} > x_{EE}$ (indicating the intention to leave contact with the wall) at the end of the motion. The results of this experiment are presented in Fig. 11. In these figures, oscillations in tendon tensions and the force applied to the wall can be observed during the transitions between PCTC and PHFMC (Figs. 11a and 11d) when the robot comes into contact with the wall. This was also observed in simulation in [33]. Outside these transitions, during the motion, the force applied to the wall along the x-axis is around the desired value of 3 N (Fig. 11d). Forces along the y-axis due to friction on the wall are also observed. The trajectory along the y-axis is followed using PHFMC, with some oscillations caused by unmodeled nonlinear friction effects in the robot (Fig. 11c). This experiments can be viewed in the multimedia attachment "video1".

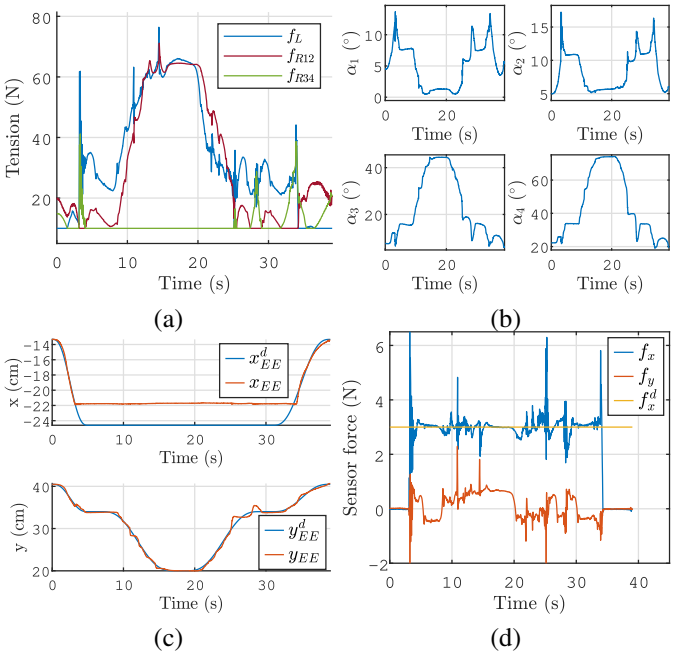

Fig. 11. Time histories of (a) $\boldsymbol{f}$, (b) $\boldsymbol{\alpha}$, (c) $\boldsymbol{q}$ and (d) expressed as functions of the position error for the PHFMC with $q_p = y_{EE}$ and $q_f = x_{EE}$. f_x and f_y are the sensor forces along the x-axis and y-axis in the world frame and f^d_x is the desired forces along the x-axis. The colors of $\boldsymbol{f}$ correspond to the tendon colors of Fig. 2

Thus, the PHFMC is indeed stable and enables the application of a force in one direction while simultaneously following a trajectory in another direction.

C. Experiments with the admittance control coupled with the PCTC

1) Admittance control interacting with a wall:
Admittance control is now used to apply the force to the wall. We set $\mathbf{M}^d_q = 2\mathbf{I}$ N/(m/s²), $\mathbf{D}^d_q = 20\mathbf{I}$ N/(m/s), and $\mathbf{K}^d_q = 100\mathbf{I}$ N/m, and the desired x-position of the EE is set to 0.03 m behind the wall in order to apply a 3 N force to the wall. The results of this experiment are shown in Fig. 12.

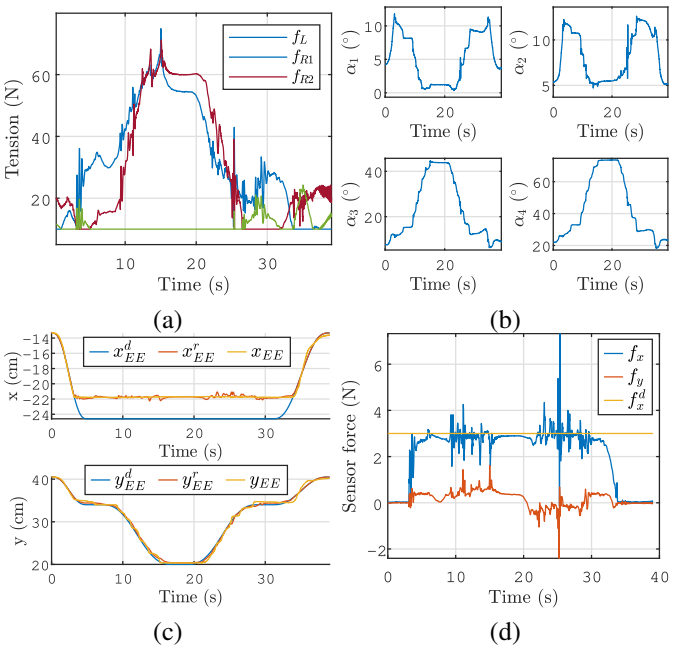

Fig. 12. Time histories of (a) $\boldsymbol{f}$, (b) $\boldsymbol{\alpha}$, (c) $\boldsymbol{q}$ and (d) expressed as functions of the position error for the admittance control interacting with a wall with $\mathbf{M}^d_q = 2\mathbf{I}$ N/(m/s²) $\mathbf{D}^d_q = 20\mathbf{I}$ N/(m/s) $\mathbf{K}^d_q = 100\mathbf{I}$ N/m. f_x and f_y are the sensor forces along the x-axis and y-axis in the world frame. The colors of $\boldsymbol{f}$ correspond to the tendon colors of Fig. 2

Figure 12c shows that although x^d_{EE} is behind the wall, x^r_{EE} stops at the wall thanks to the force feedback. As with the PHFMC, the robot therefore applies the desired force of magnitude $K^d_{x_{EE}}(x^r_{EE} - x^d_{EE})$ to the wall while simultaneously following its desired trajectory perpendicular to the wall. Figures 12a and 12d also show that there is less impact on the tendon tensions and the force applied to the EE when the robot makes or breaks contact with the wall, compared to the PHFMC control. This is because, in the case of PHFMC, there is a switch between PCTC and PHFMC, whereas admittance control involves no such switching and maintains continuous behavior. This experiments can be viewed in the multimedia attachment "video2".

Figure 13 highlights that friction affects the reference controlled variables, and thus the trajectory tracking of the position-controlled variables. It can be observed in this figure that the variation in the error between the desired and reference EE vertical position corresponds to the variation in the friction force along the wall. Indeed, for a constant friction force f_y, admittance control results in a steady-state error of $\left(K^d_{y_{EE}}\right)^{-1} f_y$. This was also observed in simulation in [33] and it was showed that this error can be reduced by increasing the value of $K^d_{y_{EE}}$.

2) Robot controlled by the hand of a user:
We are now interested in the cobotic application where a user would control the robot by applying forces on the sensor. For this, the term $\mathbf{K}^d_q$ is set to zero in the admittance control. The user then imposes a trajectory, as shown in Fig. 14, moving from configurations 1 to 6 and then approximately back to configuration 1.

We use $\mathbf{M}^d_q = 2\mathbf{I}$ N/(m/s²), Figs. 15, 16, and 17 show the robot behavior with $\mathbf{D}^d_q = 5\mathbf{I}$ N/(m/s), $\mathbf{D}^d_q = 40\mathbf{I}$ N/(m/s), and

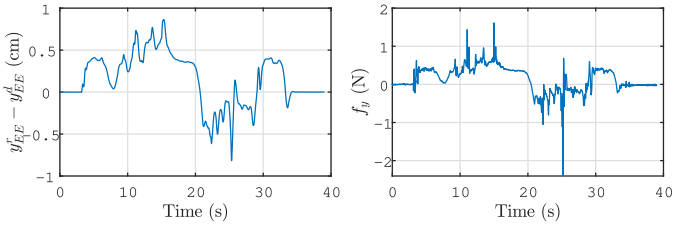

Fig. 13. Evolution of the error on the vertical reference position compared to the vertical force applied on the EE.

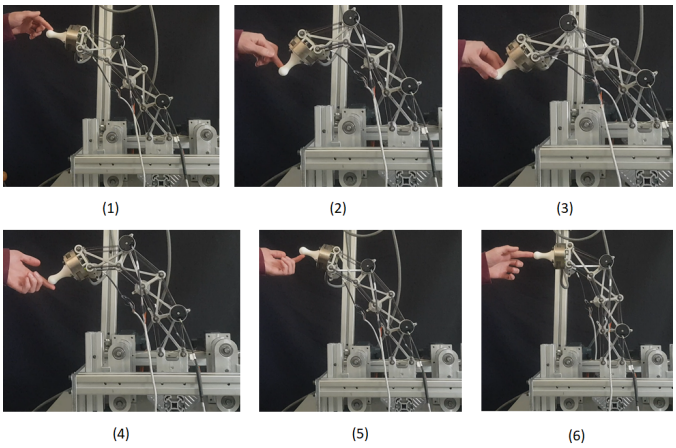

Fig. 14. Trajectory imposed by the user.

$\mathbf{D}_q^d = 100\mathbf{I}$ N/(m/s), respectively. $\mathbf{D}_q^d$ models the damping on the sensor velocity in this context. In all three cases, it can be observed that the control is stable and that the user manages to make the robot follow its motion. However, when the damping is low, the EE motion oscillates significantly in the user hand, as shown in Figs. 15c and 15d, compared to higher damping values in Figs. 16c, 16d, 17c, and 17d. These oscillations propagate throughout the entire robot, as shown in Figs. 15a and 15b. If the damping is too high, the user needs to apply more force to move the robot, as shown in Fig. 17d compared to lower damping in Fig. 16d. It is therefore necessary to choose the damping appropriately to ensure user comfort and ergonomics. An example of the application of this admittance control can be viewed in the multimedia attachment "video3".

VI. Discussions

The control laws proposed here have a low computational cost. Using MATLAB on a computer equipped with an Intel(R) Core(TM) Ultra 7 165H processor (3.8 GHz, 16 cores, 22 logical processors), the PHFMC is computed in approximately 40 μs and the admittance control in 60 μs, including about 30 μs required for the computation of the dynamic terms. The computation of the matrix $\mathbf{P}$, obtained through a singular value decomposition, has a complexity of $\mathcal{O}(N_j N_c^2)$. Similarly, the computation of the null space of $\mathbf{PZ}$ has a complexity of $\mathcal{O}(N_c(N_j - N_c)^2)$. In our case, with a single degree of actuation redundancy, the TDA has a complexity of $\mathcal{O}(N_c)$. Therefore, this control scheme can be implemented at high frequency on more complex systems.

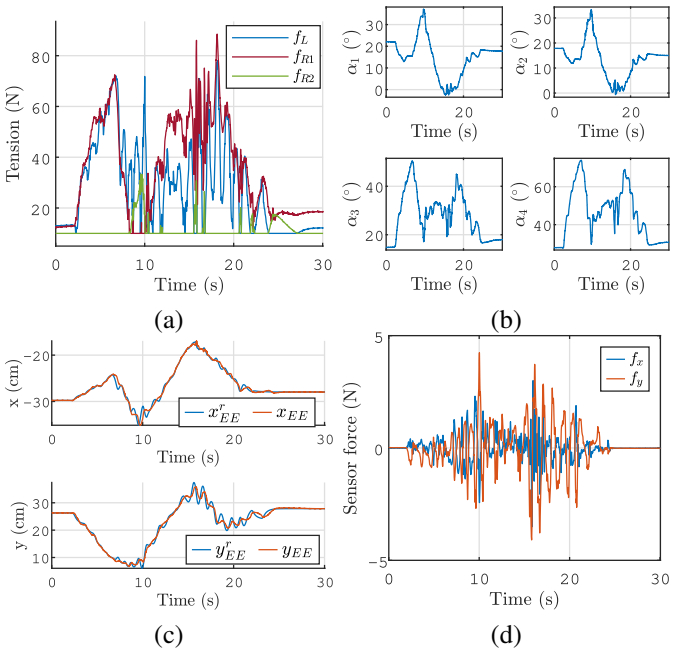

Fig. 15. Time histories of (a) $\boldsymbol{f}$, (b) $\boldsymbol{\alpha}$, (c) $\boldsymbol{q}$ and (d) expressed as a functions of the position error for the admittance control interacting with a user with $\mathbf{M}_q^d = 2\mathbf{I}$ N/(m/s²) $\mathbf{D}_q^d = 5\mathbf{I}$ N/(m/s) $\mathbf{K}_q^d = 0\mathbf{I}$ N/m. f_x and f_y are the sensor forces along the x and y axis in the world frame. The colors of $\boldsymbol{f}$ correspond to the tendon colors of Fig. 2

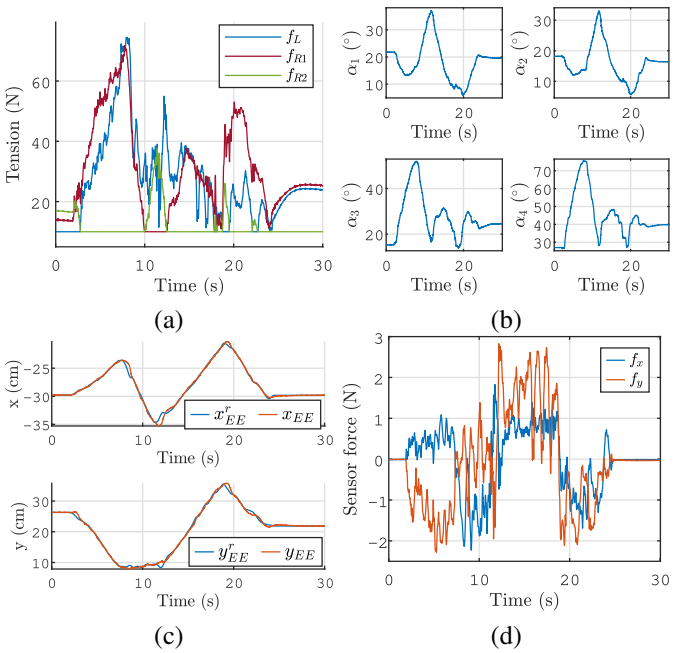

Fig. 16. Time histories of (a) $\boldsymbol{f}$, (b) $\boldsymbol{\alpha}$, (c) $\boldsymbol{q}$ and (d) expressed as a functions of the position error for the admittance control interacting with a user with $\mathbf{M}_q^d = 2\mathbf{I}$ N/(m/s²) $\mathbf{D}_q^d = 40\mathbf{I}$ N/(m/s) $\mathbf{K}_q^d = 0\mathbf{I}$ N/m. f_x and f_y are the sensor forces along the x and y axis in the world frame. The colors of $\boldsymbol{f}$ correspond to the tendon colors of Fig. 2

We also showed in [33] that these control laws remain stable even at lower control update frequencies ($dt = 10$ ms). Furthermore, [33] demonstrates that when the wall is not perfectly rigid but has a finite stiffness, the proposed admittance control remains stable. However, in this case, instability issues may arise with the PHFMC. It was also observed in

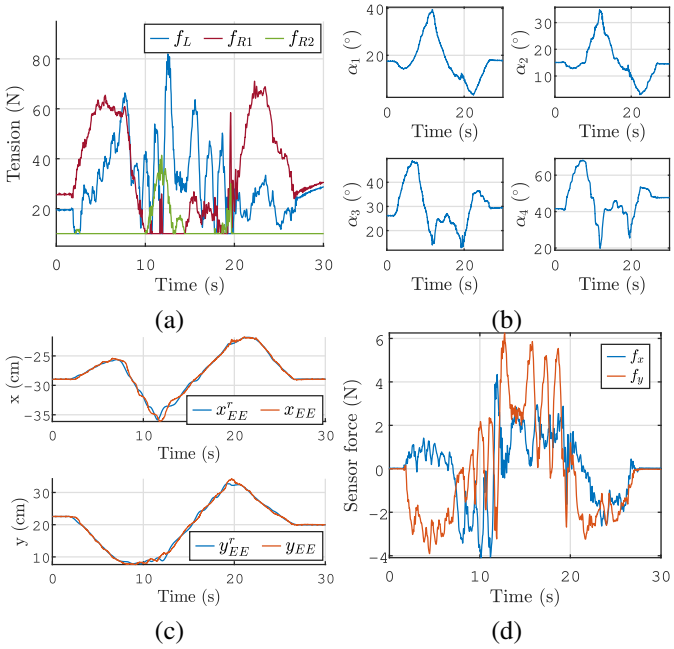

Fig. 17. Time histories of (a) $\boldsymbol{f}$, (b) $\boldsymbol{\alpha}$, (c) $\boldsymbol{q}$ and (d) expressed as a functions of the position error for the admittance control interacting with a user with $\mathbf{M}_q^d = 2\mathbf{I}$ N/(m/s²) $\mathbf{D}_q^d = 100\mathbf{I}$ N/(m/s) $\mathbf{K}_q^d = 0\mathbf{I}$ N/m. f_x and f_y are the sensor forces along the x and y axis in the world frame. The colors of $\boldsymbol{f}$ correspond to the tendon colors of Fig. 2

[33] that instabilities may arise in the presence of a large Coulomb friction coefficient. The stability of the PHFMC is more sensitive to this coefficient than that of the admittance control.

A difficulty associated with admittance control is the need for accurate knowledge of the wall properties (position and stiffness) in order to effectively apply the desired force. It can also be noted that contacts occurring at locations other than the end-effector have not been considered. Such contacts could also affect the performance and stability of both control strategies. Finally, the stability analysis was conducted starting from a static configuration. Different stability results may be obtained in the stability analysis if high velocities are considered.

VII. Conclusion

This paper addressed force control strategies based on the pseudo computed torque control (PCTC) framework for an underactuated tendon-driven robot inspired by the bird neck and composed of X-joints, where underactuation results from multiple joints sharing the same tendons. Analytical transfer matrices of the linearized system were derived for each strategy, and pole analysis was used to assess stability.

A pseudo hybrid force/motion control (PHFMC) scheme, based on the PCTC framework, was proposed to regulate both position-controlled variables and force-controlled variables, and its stability was demonstrated during robot–wall contact. Admittance control combined with PCTC, which generates forces based on position error, was also investigated for wall force regulation and collaborative motion tracking. Stability was ensured in both cases, subject to a condition on the virtual mass $\mathbf{M}_q^d$ in the wall-contact scenario.

Experiments validated the stability of the proposed approaches. Controller switching between PCTC and PHFMC during contact transitions was shown to induce disturbances, whereas admittance control avoids switching but requires accurate wall position knowledge for precise force tracking. Wall friction, although limited in the experiments, was found to degrade admittance-based position tracking more than PHFMC. In cobotic interaction, proper tuning of $\mathbf{D}_q^d$ was identified as essential for user comfort.

Future work will extend the stability analysis to robots with more joints, investigate the addition of an extra tendon for end-effector orientation control, and evaluate the impact of introducing a base revolute joint enabling spatial motion.

References

[1] B. Fasquelle, M. Furet, C. Chevallereau, and P. Wenger, "Dynamic modeling and control of a tensegrity manipulator mimicking a bird neck," in *Advances in Mechanism and Machine ScienceProceedings of the 15th IFToMM World Congress on Mechanism and Machine Science*, Springer International Publishing, 2019, pp. 2087–2097.

[2] B. Fasquelle et al., "Identification and Control of a 3-X Cable-Driven Manipulator Inspired From the Bird's Neck," *Journal of Mechanisms and Robotics*, vol. 14, no. 1, Feb. 2022, Publisher: American Society of Mechanical Engineers.

[3] H. Stachel, "Flexible cross-polytopes in the euclidean 4-space," *Journal for Geometry and Graphics*, vol. 4, Feb. 2001.

[4] N. J. Testard, C. Chevallereau, and P. Wenger, "Comparison analysis of bio-inspired tendon-driven manipulators based on their tension-feasible workspace," *Journal of Mechanisms and Robotics*, vol. 17, no. 1, 2025.

[5] N. J. Testard, C. Chevallereau, and P. Wenger, "Control analysis of an underactuated bio-inspired robot," *Robotica*, pp. 1–25, 2024. DOI: 10.1017/S0263574724001103

[6] M. Li, R. Kang, S. Geng, and E. Guglielmino, "Design and control of a tendon-driven continuum robot," *Transactions of the Institute of Measurement and Control*, vol. 40, no. 11, pp. 3263–3272, 2018.

[7] F. Janabi-Sharifi, A. Jalali, and I. D. Walker, "Cosserat rod-based dynamic modeling of tendon-driven continuum robots: A tutorial," *IEEE Access*, vol. 9, pp. 68 703–68 719, 2021.

[8] N. J. Testard, C. Chevallereau, and P. Wenger, "Dynamics and computed torque control stability of an under-actuated tendon-driven manipulator," in *Advances in Mechanism and Machine Science*, M. Okada, Ed., ser. Proceedings of the 16th IFToMM World Congress 2023 — Volume 2, Cham: Springer Nature Switzerland, 2023, pp. 332–341.

[9] D. Chen and B. Paden, "Stable inversion of nonlinear non-minimum phase systems," *International Journal of Control*, vol. 64, no. 1, pp. 81–97, May 1996.

[10] Y. Aoustin, C. Chevallereau, A. Glumineau, and C. Moog, "Experimental results for the end-effector control of a single flexible robotic arm," *IEEE Transactions on Control Systems Technology*, vol. 2, no. 4, pp. 371–381, Dec. 1994.

[11] A. A. Kumar, J.-F. Antoine, and G. Abba, "Control of an Underactuated 4 Cable-Driven Parallel Robot using Modified Input-Output Feedback Linearization," en, *IFAC-PapersOnLine*, vol. 53, no. 2, pp. 8777–8782, Jan. 2020, 21st IFAC World Congress.

[12] L. Villani and J. De Schutter, "Force Control," en, in *Springer Handbook of Robotics*, B. Siciliano and O. Khatib, Eds., Cham: Springer International Publishing, 2016, pp. 195–220.

[13] N. Hogan, "Impedance control: An approach to manipulation: Part ii—implementation," *Journal of Dynamic Systems, Measurement and Control*, vol. 107, 1985.

[14] T. Wimbock, C. Ott, A. Albu-Schaffer, A. Kugi, and G. Hirzinger, "Impedance control for variable stiffness mechanisms with nonlinear joint coupling," in *2008 IEEE/RSJ International Conference on Intelligent Robots and Systems*, 2008, pp. 3796–3803.

[15] R. Ozawa, K. Hashirii, Y. Yoshimura, M. Moriya, and H. Kobayashi, "Design and control of a three-fingered tendon-driven robotic hand with active and passive tendons," en, *Autonomous Robots*, vol. 36, no. 1, pp. 67–78, Jan. 2014.

[16] J. Duan, K. Zhang, K. Qian, J. Hao, Z. Zhang, and C. Shi, "An operating stiffness controller for the medical continuum robot based on impedance control," *Cyborg and Bionic Systems*, vol. 5, p. 0110, 2024.

[17] G. Nazmara, M. M. Fateh, and S. M. Ahmadi, "A model-reference impedance control of robot manipulators using an adaptive fuzzy uncertainty estimator," *International Journal of Computational Intelligence Systems*, vol. 11, no. 1, pp. 979–990, 2018.

[18] M. Métillon, "Modelling, control and performance analysis of cable-driven parallel cobots," Ph.D. dissertation, École centrale de Nantes, 2023.

[19] A. Fortin-Côté, P. Cardou, and C. Gosselin, "An admittance control scheme for haptic interfaces based on cable-driven parallel mechanisms," in *2014 IEEE International Conference on Robotics and Automation (ICRA)*, 2014, pp. 819–825.

[20] M. C. Yip and D. B. Camarillo, "Model-less hybrid position/force control: A minimalist approach for continuum manipulators in unknown, constrained environments," *IEEE Robotics and Automation Letters*, vol. 1, no. 2, pp. 844–851, 2016.

[21] S. Xu, B. He, Y. Zhou, Z. Wang, and C. Zhang, "A hybrid position/force control method for a continuum robot with robotic and environmental compliance," *IEEE Access*, vol. 7, pp. 100 467–100 479, 2019.

[22] M. Mistry and L. Righetti, "Operational space control of constrained and underactuated systems," in *Robotics: Science and systems*, vol. 7, 2012, pp. 225–232.

[23] H. K. Khalil, "Lyapunov's stability theory," in *Encyclopedia of Systems and Control*, J. Baillieul and T. Samad, Eds., Springer London, 2015, pp. 685–690.

[24] V. Santibáñez and R. Kelly, "Strict lyapunov functions for control of robot manipulators," *Automatica*, vol. 33, no. 4, pp. 675–682, 1997.

[25] R. J. Beerends, H. G. ter Morsche, J. C. van den Berg, and E. M. van de Vrie, *Fourier and Laplace Transforms*. Cambridge University Press, 2003.

[26] H. K. Khalil, *Nonlinear systems*. Prentice Hall, 2002.

[27] N. J. Testard, "Implementation of a tendon-driven, underactuated tensegrity robot inspired by the bird neck," Ph.D. dissertation, École centrale de Nantes, 2024.

[28] S. Kawamura and K. Ito, "A new type of master robot for teleoperation using a radial wire drive system," in *Proceedings of 1993 IEEE/RSJ International Conference on Intelligent Robots and Systems (IROS'93)*, IEEE, vol. 1, 1993, pp. 55–60.

[29] N. J. Testard, C. Chevallereau, and P. Wenger, "Static analysis of an under-actuated bio-inspired robot," Laboratoire des sciences du numérique de Nantes (LS2N), Tech. Rep., 2024.

[30] B. Rasof, "The initial- and final-value theorems in Laplace transform theory," en, *Journal of the Franklin Institute*, vol. 274, no. 3, pp. 165–177, Sep. 1962.

[31] K. Kronander and A. Billard, "Stability considerations for variable impedance control," *IEEE Transactions on Robotics*, vol. 32, no. 5, pp. 1298–1305, 2016.

[32] R. Bonitz and T. C. Hsia, "Internal force-based impedance control for cooperating manipulators," *IEEE Transactions on Robotics and Automation*, vol. 12, no. 1, pp. 78–89, 1996.

[33] N. J. S. Testard, C. Chevallereau, and P. Wenger, "Application of force control strategies on an underactuated tendon-driven robot in simulation," Lirmm, University of Montpellier ; LS2N-Nantes Université, Tech. Rep., 2026. [Online]. Available: https://hal.science/hal-05548359

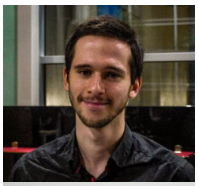

Nicolas J. S. Testard received the M.S. degree in control and robotics in 2021 and the Ph.D. degree in robotic in 2024 from Ecole Centrale de Nantes. He is currently a researcher at Laboratoire d'Informatique, de Robotique et de Microélectronique de Montpellier (LIRMM) at Montpellier, France.

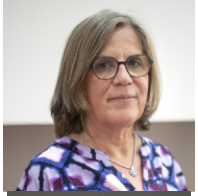

Christine Chevallereau received the master's and Ph.D. degrees from Ecole Nationale Supérieure de Mécanique, Nantes, France, in 1985 and 1988, respectively. Since 1989, she has been with the CNRS. She is currently in the Laboratoire des Sciences du Numérique de Nantes (LS2N). In 2025, she was awarded the CNRS Silver Medal. Her research interests include modeling and control of manipulators and locomotor robots, in particular biped, bio-inspired robot and robot driven by cables.

Philippe Wenger received the M.S. degree in robotics in 1985 and the Ph.D. degree in robotic in 1989 from Ecole Centrale de Nantes. He is currently a Director of Research at Centre National de la Recherche Scientifique, Laboratoire des Sciences du Numérique (LS2N), Nantes, France. His research interest include the performance analysis and evaluation of robots, the optimal design of parallel manipulators and robots, bio-inspired design and control of innovative robots.